First-principles investigation of the cooperative Jahn-Teller effect for octahedrally coordinated transition-metal ions

C. A. Marianetti,[1] D. Morgan,[1] and G. Ceder[1,2]

[1]*Department of Materials Science and Engineering, Massachusetts Institute of Technology, Cambridge, Massachusetts 02139*
[2]*Center for Materials Science and Engineering, Massachusetts Institute of Technology, Cambridge, Massachusetts 02139*

Fundamental aspects of the cooperative Jahn-Teller effect are investigated using density functional theory in the generalized gradient approximation. $LiNiO_2$, $LiMnO_2$, and $LiCuO_2$ are chosen as candidate materials as they possess small, intermediate, and large cooperative Jahn-Teller distortions, respectively. The cooperative distortion is decomposed into the symmetrized-strain modes and $k=0$ optical phonons, revealing that only the E_g and A_{1g} strain modes and E_g and A_{1g} $k=0$ optical-phonon modes participate in the cooperative distortion. The first-principles results are then used to find values for the cooperative Jahn-Teller stabilization energy and the electron-strain and electron-phonon coupling. It is found that the dominant source of anisotropy arises from the third-order elastic contributions, rather than second-order vibronic contributions. Additionally, the importance of higher-order elastic coupling between the E_g and A_{1g} modes is identified, which effectively causes expansion of A_{1g}-type modes and allows for a larger E_g distortion. Finally, the strain anisotropy induced by the antiferromagnetically ordered states is shown to cause a significant difference in the cooperative Jahn-Teller stabilization energy for the different orientations of the cooperative distortion.

I. INTRODUCTION

A. General background

The cooperative Jahn-Teller distortion is an energetic instability of the crystal structure with respect to certain modes of distortion due to electronic degeneracy. In magnetic oxides, the cooperative Jahn-Teller distortion is linked to many important phenomena. In $LaMnO_3$, for example, the Jahn-Teller distortion plays a strong role in stabilizing the A-type antiferromagnetic ordering.[1] Jahn-Teller ordering has also been invoked to understand charge ordering in these compounds.[2] Additionally, the Jahn-Teller distortion has practical consequences in electrode materials for rechargeable Li batteries. In $LiMnO_2$ and $LiNiO_2$, the transition-metal ions in the electrode material are cycled between Jahn-Teller active and inactive valence states during the charging and discharging of the battery. The resulting nonuniform volume and cell distortions can lead to rapid mechanical degradation of the electrode.[3]

In this paper, we study in detail the Jahn-Teller activity of Mn^{3+}, Ni^{3+}, and Cu^{3+} in octahedral environments. In particular, they are studied in the layered ($R\bar{3}m$) and spinel-like ($Fd\bar{3}m$) structures, which are observed in $LiMnO_2$ and $LiNiO_2$. Although the active octahedra in these ordered rock salts are edge sharing, the more general aspects of the results probably also apply to the perovskite structures that have corner-sharing octahedra.

Ligand field theory demonstrates that the d orbitals of a transition-metal ion in an octahedral complex will be split into a set of threefold degenerate t_{2g} states and twofold degenerate e_g states (see Fig. 1).[4] Both the t_{2g} and the e_g states are split under E_g-type octahedral distortions, commonly referred to as Q_2 and Q_3 (see Fig. 4). All the systems investigated in this study have filled, or half-filled, t_{2g} states so their splitting will not be considered hereafter. Splitting the

e_g states creates an electronic reduction in energy for materials with partially occupied e_g states, allowing for the distortion to operate until the increase in elastic energy halts the distortion. Ni^{3+}, Mn^{3+}, and Cu^{3+} are all susceptible to E_g-type Jahn-Teller distortions. The Jahn-Teller active spin configuration for each ion is pictured below (see Fig. 1). Note that Mn^{3+} is high spin while Ni^{3+} and Cu^{3+} are low spin. In the high-spin state, splitting the e_g states will allow Mn^{3+} to realize a decrease in energy, while Ni^{3+} and Cu^{3+} will not. In the low-spin configuration, Ni^{3+} and Cu^{3+} will realize a decrease in energy while Mn^{3+} will not. Strictly speaking, Cu^{3+} is not Jahn-Teller active because the E_g symmetry is broken when the interelectronic interaction is accounted for.[4] However, if the splitting due to the interelectronic interaction is small, this ion may still be susceptible to a pseudo-Jahn-Teller effect and the energy levels will be further split by the distortion. This is the case for $LiCuO_2$, which is found to have a strong cooperative Jahn-Teller distortion in experiment.

The previous discussion pertains to a system with discrete energy levels, such as a molecule or a Jahn-Teller defect. However, the discussion above is completely applicable to the Jahn-Teller effect in solids with somewhat localized electrons. In solids with octahedrally coordinated transition metals, a set of bonding (e_g) and antibonding (e_g^*) bands will be
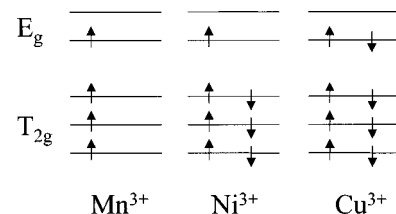
FIG. 1. Jahn-Teller active spin states.

TABLE I. Space group and Wyckoff positions of the structures evalated in this study.

Structure	Schöenflies	International	#	Li Site	Metal site	O site
Layered (rhombohedral)	D_{3d}^5	$R\bar{3}m$	166	b	a	$2c$
Layered (monoclinic)	C_{2h}^3	$C2/m$	12	$2d$	$2a$	$4i$
Spinel (cubic)	O_h^7	$Fd\bar{3}m$	227	$16c$	$16d$	$32e$
Spinel (tetragonal)	D_{4h}^{19}	$14_1/amd$	141	$8d$	$8c$	$16h$

formed, with the antibonding bands consisting primarily of metal orbitals and the bonding bands consisting primarily of oxygen p orbitals. The t_{2g} orbitals form nonbonding bands. Therefore, the valence electrons of transition-metal oxides will occupy the t_{2g} bands and the e_g^* bands. The cooperative distortion of all the octahedra, in the Q_2 or Q_3 mode, will result in the splitting of the e_g^* bands. However, there are several important differences in the solid. For the solids investigated in this study, the Jahn-Teller-active octahedra share edges and thus they do not distort independently. Whether or not the octahedra share edges, a given octahedra will feel a strain due to the distortion of the neighboring octahedra. This is known as the electron-vibrational interaction.

Additionally, magnetic and qaudrupole interactions may exist between the Jahn-Teller centers. All of these interactions may cause the distortions of different octahedra to order and become cooperative.[5] Above a critical temperature, the entropic contribution to the free energy will overcome the energetic benefit of ordering the octahedra and the distortion will become noncooperative. Additionally, the bandwidth will create other differences between the isolated and cooperative Jahn-Teller distortions, which are discussed in Sec. III B.

To study the Jahn-Teller distortion for these ions, we chose to perform calculations for $LiNiO_2$, $LiMnO_2$, and $LiCuO_2$ in the layered rhombohedral ($R\bar{3}m$) structure and its distorted variant, monoclinic ($C2/m$), because of their im-

portance as cathode materials in rechargeable Li batteries. Additionally, calculations are performed for the spinel-like cubic ($Fd\bar{3}m$) structure and its distorted variant, tetragonal ($I4_1/amd$). A summary of the space groups and Wyckoff positions for both structures is given in Table I. The general conclusions of this study are similar for the layered and spinel structures, indicating a rather small effect of structure on the properties of the distortion.

B. Spinel-like and layered structures

The layered and spinel-like structures are both ordered rock salts (see Figs. 2 and 3). The layered structure can be envisioned as two interpenetrating face-centered-cubic lattices, with one lattice consisting of oxygen and the other lattice consisting of alternating (111) planes of Li and metal. In the $R\bar{3}m$ space group the Li and the metal ions remain fixed in the ideal rock salt positions, but the oxygen atoms have a degree of freedom allowing the whole (111) oxygen plane to relax in the $\langle 111 \rangle$ direction. Physically, this relaxation is caused by the broken symmetry induced by the Li-metal ordering. Considering the effect on the individual octahedron, this planar relaxation corresponds to the T_{2g} and the T_{1g} octahedral modes, commonly referred to as Q_4, Q_5, Q_6, and Q_{19}, Q_{20}, Q_{21}, respectively (see Fig. 4). Because the Li-metal ordering breaks the cubic symmetry and causes the oxygen atoms to relax, the point group of the a site is reduced from O_h to D_{3d} upon ordering the rock-salt lattice. If a cooperative Q_3 distortion is imposed on this structure, the space group is reduced from $R\bar{3}m$ to $C2/m$. However,
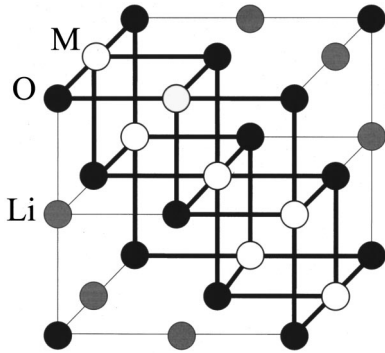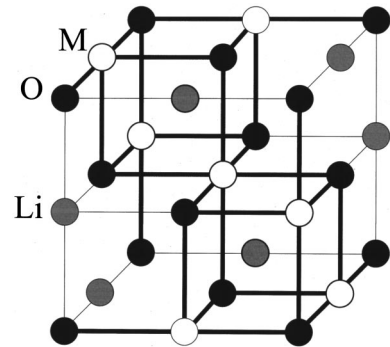

FIG. 2. Layered $LiMO_2(R\bar{3}m)$. M-O bonds are designated with thick lines. In this structure, each (111) plane is occupied by a single species. Every other (111) plane consists of oxygen, while the planes in between the oxygen planes alternate between metal and Li. The M-O octahedra share edges half with Li-O octahedra and half with other M-O octahedra. Corners of the M-O octahedra are only shared with Li-O octahedra. (Note that this is not a unit cell).

FIG. 3. Spinel $LiMO_2(Fd\bar{3}m)$. M-O bonds are designated with thick lines. As in the layered structure, corners of the M-O octahedra are only shared with Li-O octahedra. Also, the M-O octahedra share edges half with Li-O octahedra and half with other M-O octahedra. However, the M-O octahedra share different edges in the spinel and layered structures. (Note that this is not a unit cell)

$$Q_1 = \frac{x_1 - x_4 + y_2 - y_5 + z_3 - z_6}{\sqrt{6}}$$

$$Q_2 = \frac{x_1 - x_4 - y_2 + y_5}{2}$$

$$Q_3 = \frac{2 \cdot z_3 - 2 \cdot z_6 - x_1 + x_4 - y_2 + y_5}{\sqrt{12}}$$

$$Q_6 = \frac{y_1 - y_4 + x_2 - x_5}{2}$$

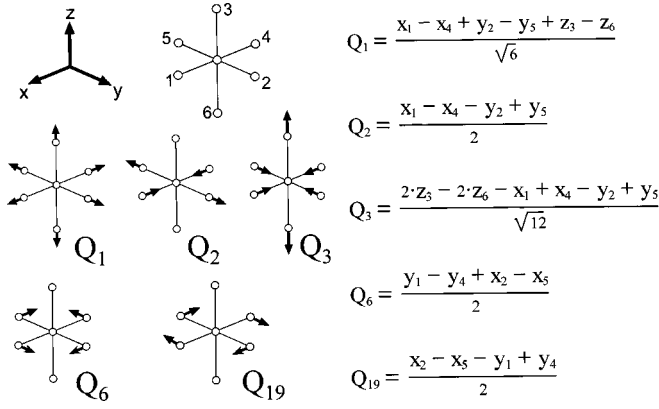$$Q_{19} = \frac{x_2 - x_5 - y_1 + y_4}{2}$$

FIG. 4. Selected symmetrized octahedral modes. The Q_2 and Q_3 modes are Jahn-Teller active.

this is still commonly referred to as the layered structure in the literature on lithium-metal oxides.

The spinel-like structure is so named due to the fact that it is synethized by lithiating $LiMn_2O_4$, which has the spinel crystal structure ($MgAl_2O_4$), to form $Li_2Mn_2O_4$. Even though the latter is not a true spinel, we shall simply refer to it as spinel, which is common in the literature on lithium-metal oxides. The spinel structure ($Fd\bar{3}m$) can be envisioned as a face-centered-cubic oxygen lattice with an interpenetrating face-centered-cubic lattice having a particular ordering of Li and metal. As in the layered structure, the Li-metal ordering breaks the cubic symmetry and causes the oxygen atoms to relax away from the ideal rock-salt positions, thus reducing the 16d site symmetry from O_h to D_{3d}.

In both these structures, the metal-oxygen octahedra share corners with Jahn-Teller inactive Li-oxygen octahedra. Edges are shared half with Li-oxygen octahedra and half with other metal-oxygen octahedra. Edge sharing between metal-oxygen octahedra will be relevant because it prevents the octahedra from distorting independently. However, the Q_2 and Q_3 components of the distortion on each metal-oxygen octahedra are independent of each other (see Sec. I C). The metal-oxygen octahedra share different edges in the spinel and layered structures. This difference will cause the cooperative distortion to be distinctly different in the two structures, and it is most likely the reason why the Jahn-Teller stabilization energy is greater in the layered structure for all three materials.

C. Cooperative Jahn-Teller distortion

The cooperative Jahn-Teller distortion can be defined as a regular ordering of local Jahn-Teller distortions. The materials examined in this study are all found to be ferrodistortive in experiment, and therefore we refer to the cooperative Jahn-Teller distortion as the imposition of identical E_g modes on each octahedron. It turns out that the E_g lattice strains and the E_g $k=0$ optical phonons are the only modes that will induce equivalent E_g distortions on each octahedron. The lattice strains are homogeneous deformations of the unit cell, while the $k=0$ optical phonons are displacements of the basis atoms. These types of symmetrized modes will now be described, and the derivation of the modes using group theory will be discussed in Sec. III C.

The E_g lattice strains are listed in Table II for the layered ($R\bar{3}m$) and spinel ($Fd\bar{3}m$) structures, and from hereon they will be referred to as the u_2 and u_3 strain modes. For spinel, the E_g strain modes are completely analogous to the octahedral modes. For example, the u_3 lattice strain in the cubic cell is compression in the X and Y directions by an amount ε and elongation in the Z direction by an amount 2ε. It is interesting to note that the E_g strain modes induce only the E_g octahedral modes on each octahedron. However, the strain modes will also distort the lattice of transition metal ions, changing the distances and angles between the transition metal ions. This will be shown to have important effects for the antiferromagnetic interaction between the transition metal ions. These statements also apply to the layered structures; however, it is slightly more complicated. Unlike spinel, the E_g representation occurs twice in the representation of the strain for the rhombohedral lattice, and therefore the layered structure has two sets of u_2 and u_3 lattice strains.

The E_g $k=0$ optical phonon modes for the layered ($R\bar{3}m$) and spinel ($Fd\bar{3}m$) structures are shown in Table III, and from hereon they will be referred to as the e_2 and e_3 optical modes. The e_3 optical mode in spinel is shown as an example in Fig. 5 and can be explained as follows. Consider fixing all the metal and Li ions and inducing a positive Q_3 octahedral distortion on all the metal-oxygen octahedra. The small vectors indicate a displacement of δ while the large vectors indicate a displacement of 2δ. Additionally, the gray arrows correspond to the Q_3 octahedral distortion of the central metal-oxygen octahedron, whereas the black arrows correspond to the Q_3 octahedral distortions of the neighboring

TABLE II. E_g and A_{1g} symmetrized strain modes for cubic (spinel) and rhombohedral (layered) lattices. The E_g and A_{1g} irreducible both occur twice in the representation of the strains for the hexagonal lattice.

	Symmetrized strain modes		
	$u_1(A_{1g})$	$u_3(E_g)$	$u_2(E_g)$
Cubic	$\frac{1}{\sqrt{3}}(\varepsilon_{xx}+\varepsilon_{yy}+\varepsilon_{zz})$	$\frac{1}{\sqrt{6}}(2\varepsilon_{zz}-\varepsilon_{yy}-\varepsilon_{xx})$	$\frac{1}{\sqrt{2}}(\varepsilon_{xx}-\varepsilon_{yy})$
Rhombohedral	$\frac{1}{\sqrt{2}}(\varepsilon_{xx}+\varepsilon_{yy})$	$\frac{1}{\sqrt{2}}(\varepsilon_{xx}-\varepsilon_{yy})$	ε_{xy}
	ε_{zz}	ε_{xz}	ε_{yz}

TABLE III. E_g and A_{1g} $k=0$ symmetrized-phonon modes for the space groups $R\bar{3}m$ and $Fd\bar{3}m$. Only the oxygen atoms participate in these modes. The position of each oxygen atom and the corresponding displacement vector is given for both space groups.

| | | $k=0$ Optical phonons | | |
	Positions	$e_1(A_{1g})$	$e_3(E_g)$	$e_2(E_g)$
$Fd\bar{3}m$	(x,x,x)	$(-1,-1,-1)$	$(1,1,-2)$	$(1,-1,0)$
(spinel)	$(x,-x+\frac{1}{4},-x+\frac{1}{4})$	$(-1,1,1)$	$(1,-1,2)$	$(1,1,0)$
	$(-x+\frac{1}{4},x,-x+\frac{1}{4})$	$(1,-1,1)$	$(-1,1,2)$	$(-1,-1,0)$
	$(-x+\frac{1}{4},-x+\frac{1}{4},x)$	$(1,1,-1)$	$(-1,-1,-2)$	$(-1,1,0)$
	$(-x,-x,-x)$	$(1,1,1)$	$(-1,-1,2)$	$(-1,1,0)$
	$(-x,x+\frac{1}{4},x+\frac{1}{4})$	$(1,-1,-1)$	$(-1,1,-2)$	$(-1,-1,0)$
	$(x+\frac{1}{4},-x,x+\frac{1}{4})$	$(-1,1,-1)$	$(1,-1,-2)$	$(1,1,0)$
	$(x+\frac{1}{4},x+\frac{1}{4},-x)$	$(-1,-1,1)$	$(1,1,2)$	$(1,-1,0)$
$R\bar{3}m$	$(0,0,z)$	$(0,0,1)$	$(2,1,0)$	$(0,1,0)$
(layered)	$(0,0,-z)$	$(0,0,-1)$	$(-2,-1,0)$	$(0,-1,0)$

metal-oxygen octahedra. Only the displacements of the oxygen atoms belonging to the center octahedron are shown. The figure indicates that the Q_3 octahedral distortion of the central octahedron is not affected by the Q_3 distortions of the other octahedra. However, the Q_3 distortion of the neighboring octahedra will create Q_4, Q_5, Q_6, Q_{19}, Q_{20}, and Q_{21} distortions in the central octahedron, which are the T_{2g} modes and the T_{1g} modes (see Fig. 4). In other words, the E_g optical modes induce local E_g octahedral distortions in addition to local T_{2g} and T_{1g} distortions, in contrast to the E_g strain modes. However, the optical E_g modes do not distort the transition metal lattice whereas the E_g strains do. It should be noted that the perovskite structure does not have E_g $k=0$ optical modes.

As will be identified later in this study (see Sec. IV B), the A_{1g} modes play an important role in the cooperative distortion. The A_{1g} irreducible representation is the identity representation.
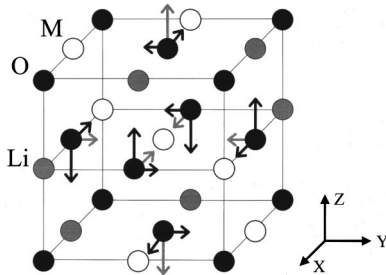

FIG. 5. The e_3 $k=0$ optical-phonon mode in the spinel structure ($Fd\bar{3}m$). The e_3 $k=0$ optical phonon can be constructed by inducing an equivalent octahedral Q_3 distortion on every M-O octahedron. The displacements in the Z direction correspond to 2δ, whereas displacements in the X and Y direction correspond to displacements of δ. The displacements are only labeled for the oxygen atoms that belong to the center M-O octahedron. Gray arrows correspond to displacements caused by the Q_3 distortion of the central M-O octahedron whereas the black arrows correspond to displacements caused by Q_3 distortions of neighboring octahedra. This figure illustrates that the Q_3 distortions of the M-O octahedra are independent of one another.

sentation, and the distortions that project onto this representation do not break the symmetry. The A_{1g} mode for the octahedron, also known as the Q_1 mode, is simply the uniform expansion or contraction of all the bond lengths (see Fig. 4). The A_{1g} strain and A_{1g} $k=0$ optical distortions will be referred to as u_1 and e_1, respectively (Tables II and III). As explained previously, the (111) oxgen planes in the layered structure can relax in the $\langle 111 \rangle$ direction and this is the e_1 $k=0$ optical phonon. As for the e_3 mode in spinel, the e_1 mode in spinel can be envisioned by inducing Q_1 octahedral distortions on each metal octahedron. The u_1 strain mode in spinel is simply a uniform expansion or contraction of the volume. There are two A_{1g} strain modes in the layered structure, u_{1a} and u_{1b}. If a hexagonal coordinate system is considered, this corresponds to a uniform expansion or contaction of the a and b lattice parameters, or a uniform expansion or contraction of the c lattice parameter.

We shall close this section with a short summary. The cooperative Jahn-Teller distortion in the layered and spinel structures, evaluated in this study, is some linear combination of E_g and A_{1g} strain modes and E_g and A_{1g} $k=0$ optical-phonon modes. The E_g strain modes and E_g $k=0$ optical-phonon modes are the only two collective distortions that will impose equivalent E_g distortions on each Jahn-Teller active octahedron. Although the A_{1g} mode exists in the direct product of the E_g irreducible representation, it is not Jahn-Teller active in the sense that it is totally symmetric and does not split the e_g levels. However, it will be demonstrated that there is a strong coupling between the A_{1g} and E_g modes that causes the A_{1g} modes to participate in the cooperative distortion.

D. Materials background

LiMnO$_2$ can be synthesized in the orthorhombic,[6] spinel,[7] and layered[8] type structures. In experiment, these systems are all found to be cooperatively Jahn-Teller distorted with the orthorhombic structure being the ground state.[6,9] The same result is found using density functional theory (DFT) in the generalized gradient approximation, although the ground

state was found to depend sensitively on the magnetic ordering.[10] Additionally, the bond lengths predicted using DFT agree well with experiment.

$LiNiO_2$ can be synthesized in the layered structure;[11] however, some small fraction of Ni atoms are found on the lithium sites and the material has not yet been synthesized stoichiometrically.[12] Layered $LiNiO_2$ displays a noncooperative Jahn-Teller distortion. X-ray diffraction data can be fit to the space group $R\bar{3}m$, which is an undistorted structure, suggesting that the Jahn-Teller distortion is not present. However, extended x-ray absorption fine structure (EXAFS) data has shown that the Ni-O octahedra are locally Jahn-Teller distorted, implying that the distortion is noncooperative.[13] This is consistent with the fact that the stabilization energy of the cooperative Jahn-Teller distortion is found to be very small in this study.

Layered $LiCuO_2$ is a relatively new material which was first synthesized in 1992. Initially, $LiCuO_2$ was incorrectly assigned to the orthorhombic structure,[14] until it was correctly identified as being layered.[15] The experimentally determined bond lengths of $LiCuO_2$ indicate the presence of an extremely large Jahn-Teller distortion, which is also found in our calculations. As far as the authors are aware, none of the publications regarding the initial synthesis of $LiCuO_2$, nor publications addressing cathode performance[16] or superconductivity[17] acknowledge the presence of the large Jahn-Teller distortion in this material.

II. OUTLINE

Previous studies have indicated that density functional theory in the generalized gradient approximation can accurately model structural aspects of the cooperative Jahn-Teller distortion in $LiMnO_2$ as compared to experiment.[10] In this study, we perform first-principles calculations for $LiMnO_2$, $LiNiO_2$, and $LiCuO_2$ for both the undistorted and cooperatively Jahn-Teller-distorted systems. To our knowledge, these are the first *ab initio* calculations that have been performed for $LiCuO_2$. The energy as a function of the Jahn-Teller distortion is calculated using density functional theory in the generalized gradient approximation, yielding the cooperative Jahn-Teller stabilization energy and the vibronic coupling for the E_g strain and phonon modes. The radial dependence of the higher-order terms will be exploited to reveal the fact that the higher-order elastic term is dominant over the higher-order vibronic term. These statements apply to both the E_g strains and optical phonons.

Additionally, the role of A_{1g}-type modes in the Jahn-Teller distortion are explored. It will be shown that the expansion of A_{1g} modes effectively allows for larger E_g distortions. Finally, the coupling between the magnetic ordering and the cooperative Jahn-Teller distortion is explored.

III. THEORY

A. The isolated Jahn-Teller center

In 1937, Jahn and Teller demonstrated that degenerate electronic states (excluding Kramers degeneracy) in a molecule will always be unstable with respect to some distortion,

with the exception of the linear molecule.[18] The distortion of an octahedron can be described exactly by the 21 octahedral modes[19] (see Fig. 4). Van Vleck used perturbation theory to explicitly solve the $E \otimes e$ Jahn-Teller problem, demonstrating that the degenerate e_g states in an octahedral complex will be split by the Q_2 and Q_3 octahedral modes.[20] In the simplest model, the Hamiltonian for an isolated octahedron or a Jahn-Teller defect in an otherwise perfect crystal can be written as a sum of elastic and electronic energy (see Ref. 4 for a detailed derivation). In the harmonic approximation, the elastic energy will be proportional to the square of the displacement, and the electronic energy can be found by perturbing the e_g states with the vibronic interaction. The lower eigenvalue of this simple Hamiltonian may be written in polar coordinates (equation 1) as follows (equation 2):

$$Q_3 = \rho \cos \phi \quad Q_2 = \rho \sin \phi \tag{1}$$

$$E = \tfrac{1}{2} k \rho^2 + F_E \rho, \tag{2}$$

where k is an elastic constant and F_E is the first-order vibronic coupling constant.

The energy can be plotted in Q_2-Q_3 space and the result is a spherically symmetric potential known as the Mexican hat potential. The minimum of this potential is a degenerate circle in Q_2-Q_3 space, indicating that all linear combinations of Q_2 and Q_3 lying on the circle are degenerate. The Q_3 mode is defined such that a positive tetragonal distortion is in the Z direction. It can be shown that the X and Y orientation of the Q_3 mode will correspond to a rotation of $2\pi/3$ and $4\pi/3$ in Q_2-Q_3 space, respectively. The same can be shown for Q_2. Because of this degenerate circle in Q_2-Q_3 space, the system can move freely along the circumference between different amplitudes and orientations of the modes.

In order to attain a higher degree of accuracy, the elastic energy can be expanded to third order[21] and the vibronic coupling can be expanded to second order[22] (see Ref. 23 for a detailed derivation). Diagnolizing this Hamiltonian and expanding to first order yields the following eigenvalue (equation 3):

$$E = \tfrac{1}{2} k \rho^2 + F_E \rho + G_E \rho^2 \cos(3\phi) + B \rho^3 \cos(3\phi), \tag{3}$$

where G_E is the second-order vibronic coupling, and B is the third-order force constant. Both the anharmonic elastic term and the second-order vibronic term end up contributing a $\cos 3\phi$ term to the energy, with the elastic term going as ρ^3 and the vibronic term going as ρ^2. This potential is known as the warped Mexican hat potential due to the fact that the spherical symmetry has been broken, reducing the potential to threefold symmetry. Intuitively, threefold symmetry must be retained due to the equivalence of the distortion in the X, Y, and Z orientations. Values of B, $G_E < 0$ support minima at $\phi = 0$, $2\pi/3$, and $4\pi/3$, while B, $G_E > 0$ support minima at $\phi = \pi/3$, $-\pi/3$, and π. Most systems are found to be distorted with a positive Q_3 distortion ($\phi = 0$).[19]

Because both higher-order elastic and vibronic terms create the same type of anisotropy in Q_2-Q_3 space, it is often ambiguous as to what the dominant source of the anisotropy is, which is evident in the early literature. Opik and Pryce

were the first to account for the anisotropy in the potential and they used only third-order elastic contributions.[21] In 1958, approximately one year later, Liehr and Ballhausen explained the anisotropy with second-order vibronic coupling disregarding the third-order elastic contributions.[22] Interestingly, the calculations they performed using crystal field theory yield a negative second-order vibronic coupling, which stabilizes the negative distortion contrary to what is normally observed in experiment. They concluded that the second-order vibronic coupling, as predicted by crystal field theory, must be treated as a phenomenological constant because their calculations predict the wrong sign. Further calculations by Ballhausen and Johansen using linear combination of atomic orbitals methods were also deemed not accurate enough to calculate the second-order vibronic coupling.[24] A later paper by Pryce *et al.* discusses both higher-order elastic and vibronic terms.[25] First, they point out that the third-order elastic term would support a positive Q_3 distortion in any reasonable potential model, due to the fact that the two M-O bonds are contracted twice as much as the other four. Second, they reason that when the covalency is small, the second-order vibronic coupling may be negative or positive by a small difference, and that it would increase with increasing covalency. We address the issue of anisotropy more quantitatively in Sec. IV C.

B. Jahn-Teller effect in a crystal

Thus far, the energetics have been considered for an isolated octahedron. The Jahn-Teller effect in a crystal is far more complicated as the e_g electrons now form energy bands and not discrete energy levels. Only a small number of high-symmetry *k-points* will be degenerate and therefore the Jahn-Teller effect in the solid is largely a pseudo-Jahn-Teller effect. The formal problem of the Jahn-Teller effect for electronic states in crystals may be addressed in the same way Jahn and Teller addressed instability in molecules. Birman analyzed the direct products of the irreducible representation of two different space groups in order to find the active phonon modes for those given space groups.[26,27] Thus, the active phonons can be found for each high-symmetry *k-point* in the first Brillouin zone. As pointed out by Englman[23] and Cracknell,[28] this formalism is severely limited by the fact that the vast majority of *k-points* in the first Brillouin are not high-symmetry points and therefore little can be concluded from group theory. A more practical treatment involves treating the Jahn-Teller effect in the solid as an array of local Jahn-Teller centers having several different types of interactions: magnetic, quadrupole, and electronic-vibrational interactions.[5] All three of these interactions may cause orbital ordering in the solid. Additionally, if there is significant electron hopping, or bandwidth, this must be included in some manner.

Kristofel' points out that when considering electron-phonon coupling in crystals, the bandwidth must be considered.[29] When considering wide bands, only select phonon modes may be active, while in the case of narrow bands phonons from the entire spectrum may be active. The appropriate limit for a given system will depend on the relative difference between the strength of the vibronic coupling and the bandwidth. The materials analyzed in this study are narrow-band materials and phonons from the entire spectrum will be active. However, we only address the ferrodistortive cooperative distortion that by definition only involves $k=0$ type distortions.

Even in narrow-band systems, finite bandwidth will have an appreciable effect. In a crystal the cooperative Jahn-Teller distortion will split energy bands that are only degenerate at a few *k-points*, not discrete energy levels as in molecules. The end result is that the change in electronic energy as a function of the cooperative distortion will be nonlinear for small distortion. This occurs for two reasons. First, bands having significant width will not split uniformly or linearly as a function of the distortion, which is essentially a result of the pseudo-Jahn-Teller effect. Simplified models have shown the electronic energy to be proportional to ρ^2 for the initial stages of the distortion.[30,31] Second, even if the bands split linearly and uniformly at each *k-point* as a function of the distortion, band overlap will cause the change in the electronic energy to be nonlinear. In this study, we find for $LiMnO_2$ that the electronic term is approximately quadratic for small distortions and transitions to linear behavior once the bands no longer overlap (see Sec. IV C). It should be noted that in this context the electronic term represents the total change in electronic energy due to the splitting of the e_g^* bands.

Kanamori was one of the first to model Jahn-Teller crystals using the phonon formalism.[32] The Hamiltonian is written in terms of the phonon modes and strain modes. A vibronic coupling coefficient is assumed for each phonon mode and for the E_g strain modes, *commonly referred to as the electron-phonon coupling and the electron-strain coupling, respectively*. He also considers the ferrodistortive case in which only the E_g strains participate, demonstrating that the potential in the space of the E_g strains has the same functional form as the warped Mexican hat potential [see equation (3)]. He does not consider E_g $k=0$ optical phonons, however, the potential of the E_g $k=0$ optical phonons will also have the same functional form as equation (3). Therefore, there will be a vibronic coupling for both the E_g strain modes and the E_g $k=0$ optical-phonon mode. In the present study, it is found that the vibronic coupling is the same for the E_g strain modes and E_g $k=0$ optical phonon modes (see Sec. IV C). However, when both the strains and the optical phonons are considered, the situation is complicated by the interaction between them.

C. Symmetrizing the crystal distortions

An arbitrary crystal distortion can be described by specifying the $3n$ atomic coordinates, where n is the number of atoms in the primitive unit cell. However, taking the proper linear combinations will yield displacement vectors that transform as the irreducible representations of the space group. These symmetrized displacement modes can readily be found using standard group-theoretical techniques and the space group of the structure. As long as a given irreducible representation only appears once in the representation of the

TABLE IV. Relative energies and structural parameters calculated in this study. All calculations were performed ferromagnetically. The zero for the energy is chosen to be the undistorted layered structure for a given compound. Experimental values are included in parentheses wherever available. Both $LiNiO_2$ and $LiCuO_2$ have small negative distortions, and in some cases they are degenerate with the undistorted structure or metastable by 1 meV.

Material	Structure type	Space group	Mode	Magnetic ordering	Energy (meV)	M-O bond lengths (Å) (4)	M-O bond lengths (Å) (2)	Volume (Å^3)	Q_1 (Å)	Q_3 (Å)
$LiNiO_2$	Layered	$R\bar{3}m$		F	0	1.98 (1.97)[11]	1.98 (1.97)	34.4 (34.0)	0.00	0.01
$LiNiO_2$	Layered	$C2/m$	$+Q_3$	F	−11	1.91 (1.91)[12]	2.14 (2.07)	34.6	0.04	0.27
$LiNiO_2$	Layered	$C2/m$	$-Q_3$	F	0	2.00	1.95	34.5	0.01	−0.05
$LiNiO_2$	Spinel	$Fd\bar{3}m$		F	1	1.98	1.98	34.5	0.00	0.00
$LiNiO_2$	Spinel	$I4_1/amd$	$+Q_3$	F	−3	1.92	2.12	34.5	0.03	0.24
$LiNiO_2$	Spinel	$I4_1/amd$	$-Q_3$	F	2	1.99	1.96	34.4	0.01	−0.02
$LiMnO_2$	Layered	$R\bar{3}m$		F	0	2.04	2.04	37.4	0.00	0.01
$LiMnO_2$	Layered	$C2/m$	$+Q_3$	F	−215	1.94 (1.92)[7]	2.40 (2.31)	38.5 (37.0)	0.12	0.54
$LiMnO_2$	Layered	$C2/m$	$-Q_3$	F	−71	2.14	1.91	37.5	0.04	−0.26
$LiMnO_2$	Spinel	$Fd\bar{3}m$		F	3	2.05	2.05	37.6	0.00	0.01
$LiMnO_2$	Spinel	$I4_1/amd$	$+Q_3$	F	−208	1.94 (1.94)[6]	2.40 (2.29)	38.5 (36.9)	0.12	0.53
$LiMnO_2$	Spinel	$I4_1/amd$	$-Q_3$	F	−67	2.13	1.91	37.6	0.04	−0.25
$LiCuO_2$	Layered	$R\bar{3}m$		F	−205	2.03	2.03	35.9	0.02	0.01
$LiCuO_2$	Layered	$R\bar{3}m$		NSP	0	2.02	2.02	35.9	0.00	0.01
$LiCuO_2$	Layered	$C2/m$	$+Q_3$	NSP	−341	1.86 (1.84)[14]	2.95 (2.76)	38.9 (37.7)	0.46	1.29
$LiCuO_2$	Layered	$C2/m$	$-Q_3$	NSP	1	2.07	1.94	35.9	0.01	−0.13
$LiCuO_2$	Spinel	$Fd\bar{3}m$		NSP	0	2.02	2.02	36.0	0.00	0.01
$LiCuO_2$	Spinel	$I4_1/amd$	$+Q_3$	NSP	−290	1.87	2.87	38.5	0.42	1.18
$LiCuO_2$	Spinel	$I4_1/amd$	$-Q_3$	NSP	−1	2.05	1.97	35.9	0.01	−0.09

group, the corresponding symmetrized modes are also normal modes or phonon modes of the crystal. For irreducible representations that appear more than once, the dynamical matrix must be used to find what linear combination of the given symmetry modes is to be used to construct the phonon. A computer code is now publicly available that will find the symmetrized displacement modes using group theoretical techniques.[33] This code was used to find the symmetrized strain modes and $k=0$ phonon modes for the spinel and layered structures in this study.

The representation for the $k=0$ phonons can be decomposed into

$$[A_{1g}(O)+E_g(O)+T_{1g}(O)+2T_{2g}(O)+A_{2u}(Li,M,O)$$
$$+E_u(Li,M,O)+2T_{1u}(Li,M,O)+T_{2u}(Li,M,O)]$$

for spinel ($Fd\bar{3}m$) and

$$[A_{1g}(O)+E_g(O)+A_{2u}(Li,M,O)+E_u(Li,M,O)]$$

for layered ($R\bar{3}m$). The representation for the strain modes can be decomposed into ($A_{1g}+E_g+T_{2g}$) for a cubic lattice and into ($2A_{1g}+2E_g$) for a rhombohedral lattice. Only E_g

and A_{1g} strain and E_g and A_{1g} $k=0$ optical-phonon modes participate in the cooperative distortion in the systems evaluated in this study.

IV. RESULTS

A. Total energy calculations

First-principles calculations using density functional theory in the generalized gradient approximation have demonstrated the ability to model the structural aspects of the cooperative Jahn-Teller distortion for $LiNiO_2$, $LiMnO_2$, and $LiCuO_2$. All energies were calculated with the Vienna Ab-initio Simulation Package (VASP).[34,35] VASP solves the Kohn-Sham equations using ultrasoft pseudopotentials.[36,37] A plane-wave basis set with a cutoff energy of 600 eV was chosen. The results compiled in Table IV were calculated using a minimum of 116 irreducible k-points for the primitive layered unit cell (4 atoms) and 29 irreducible k-points for the primitive spinel unit cell (16 atoms). Higher k-point meshes, 334 irreducible k-points for the primitive layered cell and 72 irreducible k-points for the primitive spinel cell, were tested and the total energy differed by less than 1 meV

in both cases. The tetrahedron method with Blochl corrections was used to integrate the band energy for all the results in Table IV. All other calculations in this paper were calculated with a lower-k-point mesh, eight irreducible k-points for the primitive spinel cell, and band integrations were performed using the method of Methfessel-Paxton with a smearing width of 200 meV. These changes were made in order to reduce calculation time and introduce errors of approximately 5–10 meV in the total energy, which is insignificant for the results of this study. Calculations were performed in the spinel and layered structures for the undistorted structure and the corresponding positive and negative amplitudes of the cooperative Q_3 distortion. Additionally, the energy was calculated as a function of the cooperative Q_3 distortion for all three materials with ferromagnetic spin polarization. This was performed by perturbing the undistorted structure and using the method of steepest descent to relax to the minimum. The energies, bond lengths, magnitude of the octahedral Q_3 distortion, and volume are shown in Table IV with the experimental values included in parentheses where available.

As shown, the calculations agree well with experiment. In all cases, the short bonds of the octahedron are predicted to within 1% of experiment, while the long bonds are overpredicted in all three cases with an error of 3–7% as compared to experiment. $LiNiO_2$, $LiMnO_2$, and $LiCuO_2$ serve as interesting examples of study because they possess small, intermediate, and large Jahn-Teller distortions, respectively, where the size is associated with the magnitude of Q_3 or the stabilization energy. The values of the cooperative Jahn-Teller stabilization energies (the energy of the cooperatively distorted structure minus the energy of the undistorted structure) for these materials immediately yield insight into experimental observations. Unless otherwise indicated, the ferromagnetic, layered energy values will be discussed for simplicity as all the results obey the same general trends. All energies will be given per formula unit. The stabilization energy for $LiMnO_2$ is -215 meV while the stabilization energy for $LiNiO_2$ is only -11 meV. These values are consistent with the experimental observations of a strong cooperative distortion in $LiMnO_2$ and a noncooperative distortion at room temperature in $LiNiO_2$.

We also calculated the energy as a function of the cooperative distortion. As noted in Sec. I C, the cooperative distortion consists of A_{1g} and E_g strain modes and A_{1g} and E_g $k=0$ optical phonon modes. *This is indeed found in the calculation as the only nonzero displacement projections are the A_{1g} and E_g strain modes and the A_{1g} and $E_g k=0$ optical phonons.* In order to best represent the data, we plot the energy as a function of the Q_3 octahedral mode, which will reflect the contributions of both the u_3 strain and e_3 optical modes. The curve for $LiCuO_2$ is calculated entirely low spin and will be specifically discussed below. As shown in Fig. 6, the distortion is twice as large in terms of Q_3 and 20 times more energetically stable in $LiMnO_2$ as compared to $LiNiO_2$, whereas in $LiCuO_2$ it is roughly twice as large and 1.5 times more stable than in $LiMnO_2$. Several interesting features should be noted in this plot. First, the derivatives of all the curves are close to zero for the undistorted state. This would
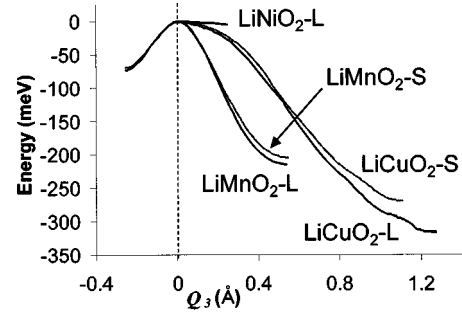

FIG. 6. Energy vs Octahedral Q_3 mode. All energies are per formula unit. These results were obtained by starting from the undistorted structure and using the method of steepest descent in order to determine the trajectory of the distortion. The energy is plotted as a function of the Q_3 octahedral distortion, which reflects contributions of both the u_3 strain mode and the e_3 $k=0$ optical-phonon mode. In all cases, the undistorted energy is referred to zero. The layered structure is designated as L while spinel is designated as S. Only $LiMnO_2$ has a significant stabilization energy in the negative distortion.

not be expected if the electronic term were linear. However, the electronic term is quadratic for small distortions because these systems are solids with finite bandwidths (see Sec. III B). Second, for a given material, the cooperative Jahn-Teller stabilization energy in the spinel structure is always less than that of the layered structure. The difference is rather small for intermediate distortions, as in $LiMnO_2$, while it increases for large distortions, as in $LiCuO_2$. Presumably, this difference is an elastic effect that arises due to the manner in which the octahedra are shared, although it is not exactly clear why the layered structure is energetically more favorable. Third, all three systems are highly anisotropic. As noted in Sec. III B, there are two sources of anisotropy when separately considering the potential of the E_g strains or the E_g $k=0$ optical phonons: vibronic anisotropy and elastic anisotropy. Both terms have a $\cos 3\phi$ dependence but the elastic term goes as ρ^3 while the electronic term goes as ρ^2. As noted in the Sec. III A, it is not immediately evident which term is causing the asymmetry. It is shown below that the dominant source of this anisotropy is the anharmonic elastic term, both for the strain and optical phonons (see Sec. IV C). Lastly, a particularly interesting feature is that $LiCuO_2$ begins with a very small slope, quite similar to that of $LiNiO_2$, but the distortion continues to grow far larger than that of $LiMnO_2$. This is due to the fact that $LiCuO_2$ has a small linear vibronic coupling but it is elastically much softer than $LiNiO_2$ and $LiMnO_2$, partially because of the presence of an extra electron in the e_g^* band.

The electronic density of states (DOS) are plotted for layered $LiMnO_2$ and $LiNiO_2$ in the undistorted and distorted structures (see Figs. 7 and 8). The energy scales are shifted such that the center of gravity of the e_g^* bands is referenced to zero. The cooperative distortion clearly splits the bands.

As stated in Sec. I A, Cu^{3+} does not have degenerate e_g electrons once the interelectronic interaction is taken into account. Within density functional theory, all of the high-symmetry k-points will display degeneracies as prescribed by
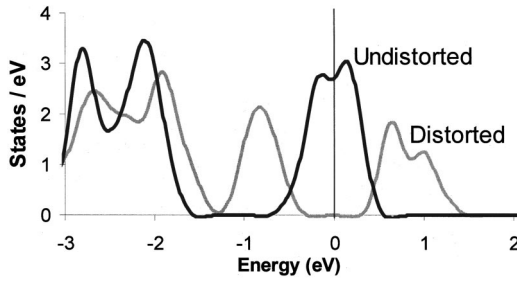
FIG. 7. Electronic DOS for distorted and undistorted layered $LiMnO_2$. The units are per formula unit. The center of gravity of the e_g^* bands is referred to zero in both cases.

the appropriate irreducible representations of the space group, and the interelectronic interaction will not break the symmetry. The concern for this is that, in reality, the electron correlation might significantly split the e_g^* bands and greatly weaken the Jahn-Teller effect. However, our calculations compare well with experiment. Therefore, it is reasonable to assume that the GGA is accurate enough to elucidate the behavior of $LiCuO_2$ reported in this work.

$LiCuO_2$ is also more complicated than the other two cases because high-spin $LiCuO_2$ is not susceptible to the Jahn-Teller distortion, nor the pseudo-Jahn-Teller distortion, whereas low-spin $LiCuO_2$ is susceptible. We shall discuss layered $LiCuO_2$ but spinel $LiCuO_2$ displays the same qualitative behavior. In the undistorted structure, the high-spin state is 205 meV lower in energy than the low-spin state (see Fig. 9). This means that the stable undistorted structure is high spin and is not Jahn-Teller active. At a value of $Q_3 = 0.3 Å$, the system transits from high spin to low spin. The distorted state is 136 meV lower in energy than the undistorted, high-spin state, and 341 meV lower than the undistorted, low-spin state. It is expected that the distortion is observed to be cooperative in experiment considering that it is stable by 136 meV with respect to the undistorted high-spin state.

B. Decomposing the cooperative distortion

The actual trajectory of the distortion has been calculated using the method of steepest descent, so the distortion can be projected onto all the symmetrized strain modes and $k=0$ optical phonons. As noted above, the only nonzero projec-
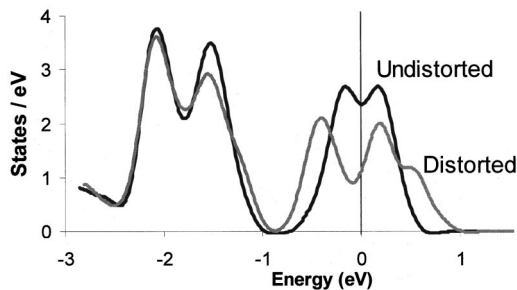

FIG. 8. Electronic DOS for distorted and undistorted layered $LiNiO_2$. The units are per formula unit. The center of gravity of the e_g^* bands is referred to zero in both cases.
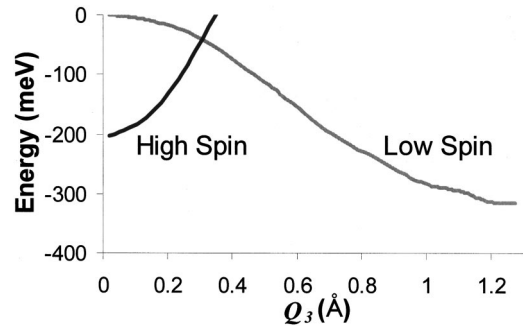

FIG. 9. Energy vs octahedral Q_3 mode for high-spin and low-spin $LiCuO_2$. The high-spin state is lower in energy than the low-spin state in the undistorted structure. However, the low-spin state is Jahn-Teller active and becomes stable over the high-spin state in the distorted structure.

tions were the A_{1g} and E_g strain modes and the A_{1g} and E_g $k=0$ optical phonons. First, the octahedral Q_3 distortion is decomposed into contributions of the u_3 strain mode and e_3 $k=0$ optical mode (see Fig. 10). In this plot, the Q_3 amplitude resulting from the u_3 strain mode is found by multiplying the normalized amplitude of the u_3 mode by a factor of $a(2\sqrt{2})^{-1}$, where a is the cubic lattice parameter, and the Q_3 amplitude resulting from the e_3 mode is found by multiplying the normalized amplitude of the e_3 mode by a factor of one half. The two individual contributions are plotted as a function of the total octahedral Q_3 distortion. Only the results for $LiCuO_2$ are shown as the decomposition is nearly identical for $LiMnO_2$ over the range of its distortion ($Q_3 = 0-0.55 Å$). At Q_3 values less than 0.5 Å, the Q_3 distortion is created largely by the lattice strains. However, as the size of the distortion increases, the optical-phonon mode begins to play a larger role.

A similar analysis can be performed to show the relative contributions of the u_1 strain mode and e_1 optical mode to the Q_1 octahedral mode. The Q_1 octahedral mode has been plotted as a function of the magnitude of the Q_3 octahedral
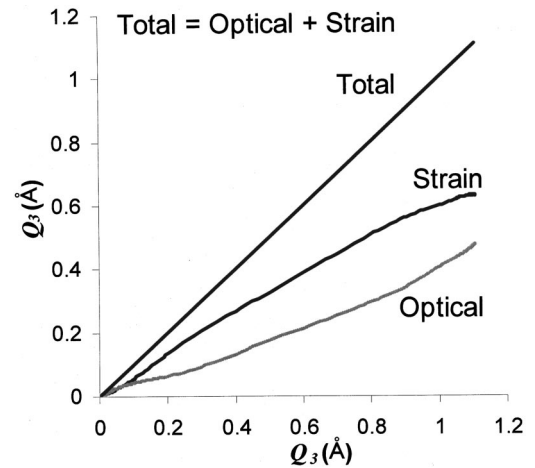

FIG. 10. The magnitude of the strain and optical contributions of the octahedral Q_3 mode are plotted vs the total magnitude of the octahedral Q_3 mode in $LiCuO_2$. As shown, the u_3 strain mode accounts for a larger portion of the octahedral Q_3 distortion.
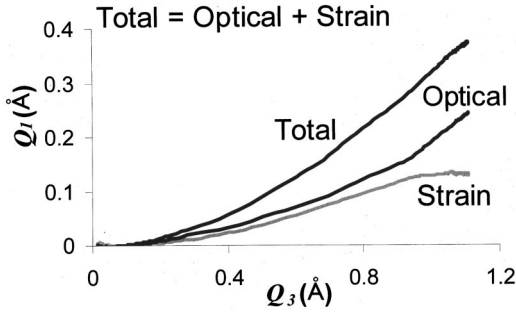
FIG. 11. The amplitude of the Q_1 octahedral distortion is plotted as a function of the Q_3 octahedral mode in LiCuO$_2$. The Q_1 octahedral distortion is further broken down into contributions from the u_1 strain mode and the e_1 $k=0$ optical phonon.

distortion for LiCuO$_2$ (see Fig. 11). Additionally, the total Q_1 distortion has been decomposed into contributions of the u_1 strain mode and e_1 $k=0$ optical-phonon mode, by multiplying the normalized modes by a factor of $a(2\sqrt{2})^{-1}$ and one half, respectively. The curves for LiMnO$_2$ and LiNiO$_2$ are similar over the ranges of their respective distortions, and therefore are not shown. The A_{1g} distortions begin to operate when the magnitude of Q_3 is approximately 0.2 Å, and scales with the size of the Q_3 distortion being very small in LiNiO$_2$ and very large in LiCuO$_2$. As shown, there is only a slightly larger contribution from the optical mode for small and intermediate distortions, corresponding to LiNiO$_2$ and LiMnO$_2$, with the optical mode becoming more dominant at large distortions. The A_{1g} strain mode is simply a uniform volume expansion, and the resulting volume expansion associated with the cooperative Q_3 distortion in the different systems is shown in Table V. The negative Q_3 distortions also induce a positive A_{1g} distortion. However, the negative Q_3 distortions are all small and therefore the resulting A_{1g} distortions are small.

The A_{1g} distortion plays an obvious role in the cooperative distortion. Recall that the octahedral Q_1 distortion is a uniform expansion or contraction of the octahedron. When the positive Q_1 distortion is superimposed with the Q_3 distortion, it cancels the inward motion of the oxygen atoms and reinforces the outward motion of the oxygen atoms. Given the proper linear combination, $\sqrt{6}Q_1+2\sqrt{3}Q_3$, two atoms

TABLE V. Percent volume expansion in going from the undistorted structure to the positive amplitude of the cooperative Q_3 distortion.

Material	Structure	% Volume change
LiCuO$_2$	Layered	8.4
LiCuO$_2$	Spinel	6.9
LiMnO$_2$	Layered	2.9
LiMnO$_2$	Spinel	2.4
LiNiO$_2$	Layered	0.6
LiNiO$_2$	Spinel	0.1

move outwards and four atoms remain stationary. For example, if the A_{1g} distortion were removed from the distorted structure of LiCuO$_2$, the short bonds would measure 1.65 Å as opposed to 1.87 Å. The results imply that the A_{1g} modes are associated with elastic anharmonicity through higher-order elastic coupling between A_{1g} and E_g (i.e., terms that go as $A_{1g}E_g^2$ and $A_{1g}^2E_g$). As noted above, Q_1 does not operate until Q_3 is approximately 0.2 Å, whereupon it becomes energetically favorable to expend energy to expand the octahedra in order to reduce the elastic energy associated with the contracted bonds from the Q_3 distortion. This makes sense physically considering that a typical interatomic potential will increase rapidly after the bond length is contracted significantly. This hypothesis is also supported by the fact that the positive Q_1 distortion is induced by both the positive and negative mode of the Q_3 distortion. The Q_1 distortion is very important in LiCuO$_2$, effectively softening Q_3 and allowing the system to distort to a much higher degree.

Previous studies have considered the role of the A_{1g} distortion. The Hamiltonian can have linear terms in A_{1g}-type distortions as the A_{1g} irreducible representation is contained within the symmetrical product of the E_g representation.[4] However, this will simply shift the e_g levels by a constant independent of the Jahn-Teller distortion because A_{1g} is totally symmetric. Van Vleck acknowledged this when he first solved the $E\otimes e$ problem, and he states that the undistorted state can be considered as equilibrated with respect to Q_1.[20] Liehr and Ballhausen used crystal field theory to perform calculations for the Jahn-Teller effect in octahedral complexes.[22] They included first-order and higher-order coupling to Q_1 when expanding the matrix elements of the Hamiltonian. A linear term in Q_1 is needed in their general Hamiltonian to describe the relative expansion or contraction of different transition metals due to the ligand field, independent of the Jahn-Teller distortion. In our calculations, there is no need to consider terms linear in A_{1g} because the structure has already been equilibrated with respect to A_{1g} distortions. Although their model does account for higher-order coupling between Q_1 and Q_3, they make no mention of the implications of this in their paper.

More recently, Atanasov et al. have considered the role of A_{1g} distortions in partially lithiated spinel Li$_x$MnO$_2$ using density functional calculations in clusters.[38] Their calculations predict that, given the Mn$_7$O$_{14}$ cluster equilibrated with respect to A_{1g} type distortions, a negative Q_1 distortion will be induced by the Q_3 distortion, which is exactly opposite to what we have found in this study. It is not completely clear why their results are qualitatively different than ours, but this is most likely due to approximations introduced in their electronic structure method. This is supported by the fact that bond lengths predicted by our calculations are more accurate as compared to experiment. The authors claim that the deviation from experiment may be due to localization being more pronounced in cluster calculations. Ultimately, the observation of Q_1 increasing with the Q_3 distortion makes more sense and the same trend is observed in LiCuO$_2$ where the effect is much more pronounced.
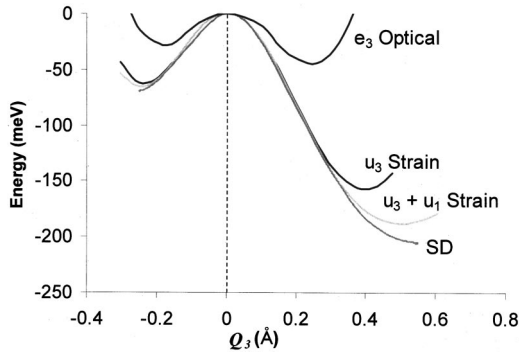
FIG. 12. Energy as a function of the octahedral Q_3 distortion in spinel $LiMnO_2$. Four different cases are considered. The steepest descent (SD) calculation represents the true trajectory of the distortion (same as calculation in Fig. 6). The u_3 strain and the e_3 optical curves show the energy as a function of the respective mode. The $u_3 + u_1$ strain curve is obtained by taking the u_3 strain curve and allowing the u_1 strain mode to relax at every point along the path (this is equivalent to relaxing the volume at every point).

In order to better understand the energetics of each phonon and strain mode, it is instructive to calculate the energy of the cooperative distortion while considering the E_g and A_{1g} strain and phonon modes separately (see Fig. 12). Separate calculations were performed for the energy as a function of the u_3 strain mode and e_3 optical mode, clearly revealing the energetic importance of the A_{1g} modes. As shown in Fig. 12 for spinel $LiMnO_2$, allowing only the u_3 strain mode reproduces the steepest descent data extremely well for distortions less than $Q_3 = 0.3$ Å. The e_3 optical mode is much less energetically favorable than the u_3 strain mode. In this study, it was found that both of these modes have the same vibronic coupling, so the observed differences must be due to differences in the elastic terms (see Sec. IV C). This decomposition explains why the E_g strain mode dominates the cooperative distortion. In order to clearly illustrate the effect of the A_{1g} mode, a calculation can be performed as a function of the u_3 strain mode, while allowing the u_1 strain mode to relax at every step. The presence of the u_1 strain mode causes the minimum to increase by 0.15 Å and the stabilization energy to increase by roughly 50 meV. When the u_1 strain mode is allowed to operate, the results are much closer to the steepest descent results with the final differences being due to the absence of the e_3 and e_1 distortions. The same analysis can be performed for $LiCuO_2$ (see Fig. 13). As for $LiMnO_2$, the cooperative distortion consisting solely of u_3 lattice strains is only accurate for small distortions. The absence of the A_{1g} modes greatly reduces the size of the distortion. Allowing the u_1 strain mode to operate greatly reduces the energy of the distortion. However, there is still a significant departure from the steepest descent curve at large distortions indicating that the e_3 and e_1 optical modes are significant in representing the energetics for large distortions.

C. Vibronic coupling of the strain modes and the optical modes

In this section, we shall discuss specific calculations that explain the differences between the distortions in the differ-
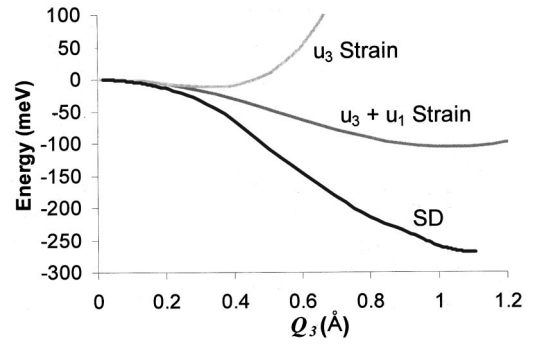

FIG. 13. Energy as a function of the octahedral Q_3 distortion in spinel $LiCuO_2$. See Fig. 12 for further description.

ent materials, the source of anisotropy in the E_g strain and E_g $k=0$ optical phonon potentials, the differences in strain and optical modes, and determine the vibronic coupling for the E_g strain and E_g $k=0$ optical phonon. Separate calculations are performed for the energy as a function of the u_3 strain distortion and the energy as a function of the e_3 optical distortion, while not allowing any A_{1g} distortions to operate. We shall only consider the spinel structure for these calculations because the E_g irreducible representation appears only once in the representation of the strains, whereas in the layered structure it appears twice. This simplifies the analysis and we expect the same conclusions to hold in both structures.

First, we examine the splitting of the e_g^* bands. We calculate the change in electronic energy by evaluating equation (4), taking the limits of integration from the lowest e_g^* state to the center of gravity of the e_g^* bands, as a function of the distortion.

$$E = \int \varepsilon \cdot D(\varepsilon) d\varepsilon. \qquad (4)$$

Because the band energies cannot be referenced absolutely for different distortions, we must assume that the center of gravity of the e_g^* states remains unchanged. Therefore, only splitting of the e_g^* bands is taken into account when calculating the change in electronic energy. As indicated in Sec. III B, the change in electronic energy for a cooperative distortion in a solid with finite bandwidth is expected to vary nonlinearly for small distortions. The change in electronic energy is plotted as a function of the positive u_3 strain distortion for all three materials (see Fig. 14). As before, the amplitude of the strain mode is multiplied by a factor of $a(2\sqrt{2})^{-1}$ such that the amplitude of the mode is equal to the induced amplitude of the Q_3 octahedral mode. This will allow us to directly compare the strain modes and optical modes below. Once the t_{2g} bands and the e_g^* bands began to overlap, no larger distortions were considered. As shown, all three curves begin nonlinearly and transition to approximately linear dependence. The nonlinear region can be accurately represented by a quadratic term, with the rms error being less than 3 meV for all three cases. The first-order vibronic coupling of the E_g strain mode can be taken as the slope of the linear portion of the curve. The vibronic cou-
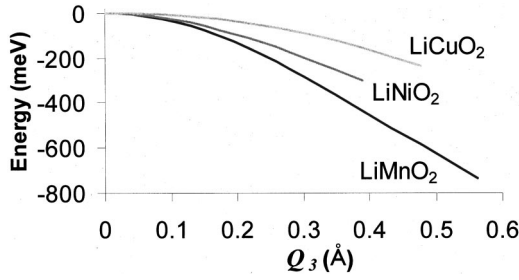
FIG. 14. Electronic energy change vs u_3 strain distortion. The change in electronic energy is calculated from the splitting of the e_g^* peaks in the DOS.

plings of the E_g strain mode for LiMnO$_2$, LiNiO$_2$, and LiCuO$_2$ are -1.70, -1.16, and -0.84 eV/Å, respectively.

Up until this point, only the vibronic coupling of the u_3 strain mode has been considered. It is also useful to calculate the change in electronic energy as a function of the e_3 optical mode. This was performed for LiMnO$_2$ and the result is nearly identical to the case of the u_3 strain mode, with all points in the nonlinear region being practically equivalent and all points in the linear region being within 15 meV of each other on a scale of 700 meV. *This indicates that the vibronic coupling of the u_3 strain mode and e_3 optical mode are practically the same*. This suggests that, to a high degree of accuracy, the change in electronic energy is only a function of the octahedral Q_3 distortion. It is also instructive to calculate the change in electronic energy for a cooperative distortion that is not ferrodistortive. This is performed by inducing a distortion in which three of the four metal-oxygen octahedra, in the primitive spinel unit cell, have octahedral Q_3 distortions in different directions but identical in magnitude. This distortion is some linear combination of $k=0$ optical phonons, and we characterize the amplitude of this mode by the magnitude of the Q_3 octahedral distortion. The result is very similar to the u_3 strain mode, with the nonlinear region being practically equivalent and the linear region having roughly the same slope but shifted by approximately -30 meV. This further illustrates that the change of electronic energy in the cooperative distortion can be approximately considered to be a function only of the Q_3 octahedral distortion. If the electrons were completely localized, this would be expected, but with the absence of the initial nonlinear behavior. However, as shown in Fig. 7 LiMnO$_2$ has a bandwidth of roughly 1 eV. The above calculations were only performed for LiMnO$_2$; however, the results are probably similar in LiNiO$_2$. Also, these arguments probably hold for small distortions in LiCuO$_2$.

The curves shown in Fig. 6 are now better understood. LiMnO$_2$ has a much larger distortion than LiNiO$_2$ because the vibronic coupling in LiMnO$_2$ is much larger than for LiNiO$_2$. Obviously, differences in elastic terms will also contribute to the differences between the two materials. Interestingly, LiCuO$_2$ has the smallest vibronic coupling, but the largest distortion and stabilization energy. This must be due to the elastic terms being much smaller in LiCuO$_2$ than in LiMnO$_2$ and LiNiO$_2$. This reasoning is supported by the

fact that there are two electrons in the antibonding e_g^* bands in LiCuO$_2$ whereas there is only one in the other two materials. It is well known that filling an antibonding band tends to decrease the elastic constants.

In order to determine the dominant source of anisotropy in the E_g strain potential, we will use two different calculations. First, we will use the same approach as above by calculating the change in electronic energy for positive and negative amplitudes of the u_3 strain distortions for LiMnO$_2$. The results for the positive and the negative amplitude are very similar, with the negative amplitude providing a slightly *larger* gain in energy. However, the calculation of the total energy indicates that the positive amplitude has a lower total energy (see Fig. 12), which must be caused by the elastic contribution. The anisotropic terms can be more accurately quantified as follows. Consider the function defined in equation (5):

$$f(\rho) = \tfrac{1}{2}[E(\rho,0) - E(\rho,\pi)]. \qquad (5)$$

This will eliminate all symmetric terms from the Hamiltonian, leaving only the second-order vibronic coupling and the third-order elastic term. This function can then be fit to a second- and third-order polynomial, revealing each term. For the u_3 mode, this gives a cubic term of -2165 eV/Å^3 and a quadratic term of 154 eV/Å^2. Considering an amplitude of 0.5 Å, the third-order elastic term is roughly seven times larger than the second-order vibronic term. The same fit was performed for the e_3 mode yielding a cubic term of -1888 eV/Å^3 and a quadratic term of 210 eV/Å^2, which behaves in the same fashion. Additionally, the fit predicts the second-order vibronic term to stabilize the negative amplitude of the u_3 distortion and the third-order elastic term to stabilize the positive amplitude of the u_3 distortion, which was also seen above when calculating the electronic energy. Therefore, we can conclude that, for these materials, the stability of the positive Q_3 distortion is due to the dominant anharmonic elastic coupling. The same trends were found for LiNiO$_2$ and LiCuO$_2$.

D. Strain anisotropy induced by antiferromagnetic ordering

Thus far, the present study has only addressed structures with ferromagnetic spin polarization. As stated in Sec. I C the E_g strain modes will distort the metal lattice. In the undistorted structure for both layered and spinel, a given transition metal will have six metal nearest neighbors. The u_3 strain mode will break the set of six nearest-neighbors into a set of four and two. In order to illustrate this, the Mn-Mn bond lengths for the six nearest neighbors are plotted versus the magnitude of the octahedral Q_3 distortion for the steepest descent calculation of the cooperative distortion in spinel LiMnO$_2$ (see Fig. 15). The positive u_3 distortion, which is defined in Z orientation (Table II), creates four long metal-metal bonds (bonds 0–2, 0–3, 0–4, and 0–5 in Fig. 16) and two short metal-metal bonds (bonds 0–1 and 0–6), while the negative distortion creates two long metal-metal bonds (bonds 0–1 and 0–6) and four short metal-metal bonds (bonds 0–2, 0–3, 0–4, and 0–5). This is opposite to how the cooperative distortion effects the metal-ligand bonds. The
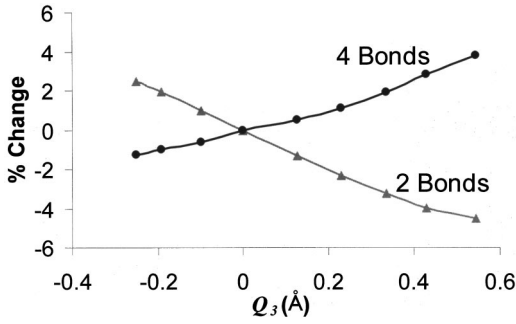
FIG. 15. Percent change in Mn-Mn bonds in spinel LiMnO$_2$ for the cooperative Q_3 distortion (steepest-descent calculation). As shown, a positive cooperative Q_3 distortion will create four long Mn-Mn bonds and two short Mn-Mn bonds due to the u_3 strain component of the distortion, while the opposite occurs for the negative cooperative Q_3 distortion. Note that this is the opposite of how the cooperative Q_3 distortion effects the Mn-O bond lengths.

magnitude of the slope of the two-bond curve is roughly 1.5 times that of the four-bond curve. The exchange interaction will be a function of the metal bond lengths, so the magnetic energy will clearly change as a function of the distortion.

The antiferromagnetic state introduces an additional complexity as compared to the ferromagnetic case. The magnetic ground state of both spinel and layered LiMnO$_2$ is antiferromagnetic, and both systems are frustrated. As shown in Fig. 16, a given metal atom can have four antiferromagnetic bonds (bonds 0–2, 0–3, 0–4, and 0–5) and two ferromagnetic bonds (bonds 0–1 and 0–6). The antiferromagnetic ordering reduces the symmetry, causing the Z orientation of the u_3 strain to be inequivalent to the X and Y orientations of the u_3 strain. For both the positive and negative cooperative distortions, it is found that the lower-energy states correspond to a deformation in which the short metal bonds are antiferromagnetic. The positive u_3 distortion creates one set of short bonds, so for the particular antiferromagnetic ordering in Fig. 16 the X and Y orientations of u_3 will result in short antiferromagnetic bonds (bonds 0–2, 0–5 and 0–3, 0–4, respectively) and the Z orientation of u_3 will result in short ferromagnetic bonds (bonds 0–1 and 0–6). The negative u_3 distortion creates four short bonds, so the Z orientation of u_3 will result in four short antiferromagnetic bonds (bonds 0–2, 0–3, 0–4, and 0–5) while the X and Y orientations of u_3 will
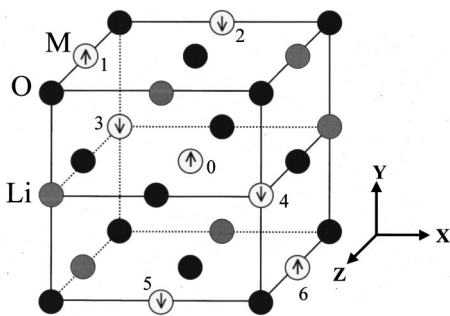

FIG. 16. The figure shows the frustrated antiferromagnetic ordering present in the spinel structure. Each M atom has four antiferromagnetic M-M bonds and two ferromagnetic M-M bonds.

TABLE VI. Relative energies of antiferromagnetic LiMnO$_2$ in different orientations of the cooperative Q_3 distortion. All energies are referenced to the undistorted, antiferromagnetic calculation. As shown, the antiferromagnetism breaks the symmetry and causes the positive X and Y orientations of the cooperative distortion to be lowest in energy. The lowest energy orientations are those which produce a maximal number of short antiferromagnetic bonds.

Orientation	Q_3 (Å)	Energy (meV)	Metal-metal bonds
X, Y	0.52	−263	2 short AF bonds
			2 long AF bonds
			2 long F bonds
Z	0.53	−194	2 short F bonds
			4 long AF bonds
$-X, -Y$	0.24	−72	2 short AF bonds
			2 short F bonds
			2 long AF bonds
$-Z$	0.24	−161	4 short AF bonds
			2 long F bonds

only create two short antiferromagnetic bonds (bonds 0–3, 0–4 and 0–2, 0–5, respectively) and two short ferromagnetic bonds (bonds 0–1, 0–6 and 0–1, 0–6). The energy was calculated for the positive and negative amplitudes of the cooperative Q_3 distortion for the X, Y, and Z orientations of the cooperative distortion in spinel LiMnO$_2$ (see Table VI). The antiferromagnetic ordering creates approximately a 70 meV difference in energy for the different orientations of the positive cooperative distortion and a 90 meV difference for the different orientations of the negative cooperative distortion. The same trends were observed in layered LiMnO$_2$. Therefore, there is a significant coupling between the magnetic ordering and the E_g strain modes, which makes certain orientations of the cooperative distortions energetically favorable.

V. CONCLUSIONS

Density functional calculations, in the generalized gradient approximation, have been used to elucidate several important aspects of the cooperative Jahn-Teller distortion for octahedrally coordinated transition-metal ions. Our calculations accurately predict the structural characteristics of the cooperative Jahn-Teller distortion in spinel and layered LiNiO$_2$, LiMnO$_2$, and LiCuO$_2$, as compared to experiment. The predicted metal-oxygen bond lengths were in reasonable agreement with experiment, having errors ranging from 1–7 %. The stabilization energy of the ferromagnetic cooperative Q_3 distortion was found to be −11, −215, and −341 meV in layered LiNiO$_2$, LiMnO$_2$, and LiCuO$_2$, respectively, and −4, −211, and −290 meV in spinel LiNiO$_2$, LiMnO$_2$, and LiCuO$_2$, respectively (see Table IV). Additionally, it was found that the Jahn-Teller distortion will induce a spin transition in LiCuO$_2$, causing the initial high-spin state to transition to low spin (see Fig. 9).

The total cooperative distortion is decomposed into the

symmetrized lattice strains and the symmetrized $k=0$ optical phonons, and it is found that only the E_g and A_{1g} strain modes and E_g and A_{1g} $k=0$ optical-phonon modes participate in the cooperative distortion. The E_g strain modes and E_g $k=0$ optical phonons both impart octahedral E_g distortions. It is found that the u_3 strain mode is responsible for the majority of the octahedral Q_3 distortion for small and intermediate Q_3 distortions while the contributions of the e_3 $k=0$ optical phonon become more important for large distortions. The A_{1g}-type modes cause all the metal-oxygen bond lengths to increase, canceling the contraction of the metal-oxygen bond lengths induced by the E_g distortions. The A_{1g}-type modes begin to operate at roughly $Q_3=0.2$ Å, whereupon it becomes energetically favorable to expend energy to expand the octahedron in order to reduce the energy associated with excessively short bond lengths (see Fig. 11). This effect is a higher-order elastic interaction between the A_{1g} and E_g modes. The importance of this effect depends on the magnitude of the Q_3 distortion, being negligible in $LiNiO_2$, intermediate in $LiMnO_2$, and extremely important in $LiCuO_2$.

The vibronic coupling of the u_3 strain mode was found to be -1.70, -1.16, and -0.84 eV/Å for spinel $LiMnO_2$, $LiNiO_2$, and $LiCuO_2$, respectively, by examining the splitting of the E_g peaks in the DOS (see Fig. 14). Additionally, it was shown that the electronic energy varies quadratically with the distortion while the E_g bands are overlapping and transits to a linear relationship thereafter. It was also found that the change in electronic energy calculated from the splitting of the DOS in $LiMnO_2$, as a function of the distortion, was essentially identical for the u_3 strain mode and the e_3 $k=0$ optical phonon mode, and very similar for a nonferrodistortive distortion. This indicates that the vibronic couplings for the u_3 strain mode and the e_3 $k=0$ optical phonon mode are practically the same, and that the change in electronic energy is approximately a function only of the magnitude of the Q_3 octahedral distortion for a cooperative distortion in $LiMnO_2$. Also, it was shown that the strong anisotropy favoring the positive amplitude of the u_3 and e_3 modes is elastic in origin, not vibronic.

Finally, it is found that symmetry breaking of the antiferromagnetically ordered state in $LiMnO_2$ can create roughly 70 meV differences in the stabilization energy for different orientations of the cooperative distortion (i.e., X, Y, or Z). This derives from the fact that the cooperative distortion significantly changes the metal-metal bond lengths, thus changing the exchange interaction.

[1] I. Solovyev, N. Hamada, and K. Terakura, Phys. Rev. Lett. **76**, 4825 (1996).

[2] K. H. Ahn and A. J. Millis, Phys. Rev. B **58**, 3697 (1998).

[3] H. Wang, Y.-L. Jang, and Y.-M. Chiang, Electrochem. Solid. State Lett. **2**, 490 (1999).

[4] I. B. Bersuker, *Electronic Structure and Properties of Transition Metal Compounds* (Wiley, New York, 1996).

[5] M. D. Kaplan and B. G. Vekhter, *Cooperative Phenomena in John-Teller Crystals* (Plenum, New York, 1995).

[6] R. Hoppe, G. Brachtel, and M. Jansen, Z. Anorg. Allg. Chem. **417**, 1 (1975).

[7] A. Yamada and M. Tanaka, Mater. Res. Bull. **30**, 715 (1995).

[8] A. R. Armstrong and P. G. Bruce, Nature (London) **381**, 499 (1996).

[9] G. Dittrich and R. Hoppe, Z. Anorg. Allg. Chem. **368**, 262 (1969).

[10] S. K. Mishra and G. Ceder, Phys. Rev. B **59**, 6120 (1999).

[11] L. D. Dyer, B. S. Borie, and G. P. Smith, J. Am. Chem. Soc. **76**, 1499 (1953).

[12] C. Delmas, J. P. Peres, A. Rougier, A. Demourgues, F. Weill, A. Chadwick, M. Broussely, F. Perton, Ph. Biensan, P. Willmann, J. Power Sources **68**, 120 (1997).

[13] A. Rougier, C. Delmas, and A. V. Chadwick, Solid State Commun. **94**, 123 (1995).

[14] K. Imai, M. Koike, H. Takei, H. Sawa, D. Shiomi, K. Nozawa, and M. Kinoshita, J. Phys. Soc. Jpn. **61**, 1819 (1992).

[15] R. Berger and L. E. Tergenius, J. Alloys Compd. **203**, 203 (1994).

[16] H. Arai, S. Okada, Y. Sakurai, and J. Yamaki, Solid State Ionics **106**, 45 (1998).

[17] F. J. Owens, Physica C **313**, 65 (1999).

[18] H. A. Jahn and E. Teller, Proc. R. Soc. London, Ser. A **161**, 220 (1937).

[19] M. D. Sturge, in *Solid State Physics*, edited by F. Seitz, D. Turnbull, and H. Ehrenreich (Academic Press, New York, 1994), Vol. 20, 91-211 (1967).

[20] J. H. Van Vleck, J. Chem. Phys. **7**, 72 (1939).

[21] U. Opik and M. H. L. Pryce, Proc. R. Soc. London, Ser. A **238**, 425 (1957).

[22] A. D. Liehr and C. J. Ballhausen, Ann. Phys. (N.Y.) **3**, 304 (1958).

[23] R. Englman, *The Jahn-Teller Effect in Molecules and Crystals* (Wiley, New York, 1972).

[24] C. J. Ballhausen and H. Johansen, Mol. Phys. **10**, 183 (1966).

[25] M. H. L. Pryce, K. P. Sinha, and Y. Tanabe, Mol. Phys. **9**, 33 (1965).

[26] J. L. Birman, Phys. Rev. **125**, 1959 (1962).

[27] J. L. Birman, Phys. Rev. **127**, 1093 (1962).

[28] A. P. Cracknell, *Group Theory in Solid-State Physics* (Taylor and Francis, London, 1975)

[29] N. N. Kirstofel', Sov. Phys. Solid State **6**, 2613 (1965).

[30] D. Adler and H. Brooks, Phys. Rev. **155**, 826 (1967).

[31] D. Adler, J. Feinleib, H. Brooks, and W. Paul, Phys. Rev. **155**, 851 (1967).

[32] J. Kanamori, J. Appl. Phys. **31**, 14s (1960).

[33] H. Stokes and D. M. Hatch, *Isotropy* (http://www.physics.byu.edu/~stokesh/isotropy.html)

[34] G. Kresse and J. Furthmuller, Phys. Rev. B **54**, 11 169 (1996).

[35] G. Kresse and J. Furthmuller, Comput. Mater. Sci. **6**, 15 (1996).

[36] D. Vanderbilt, Phys. Rev. B **41**, 7892 (1990).

[37] G. Kresse and J. Hafner, J. Phys.: Condens. Matter **6**, 8245 (1994).

[38] M. Atanasov, J.-L. Barras, L. Benco, and C. Daul, J. Am. Chem. Soc. **122**, 4718 (2000).